

Article

Lead-Free Organic Manganese (II) Bromide Hybrid with Highly Efficient and Stable Green Emission for UV Photodetection

Ye Tian ¹, Qilin Wei ^{2,*}, Lian Duan ³ and Chengyu Peng ^{3,*}¹ School of Semiconductors and Physics, North University of China, Taiyuan 030051, China² School of Chemistry and Chemical Engineering, Shandong University, Jinan 250100, China³ Traffic Information Engineering Institute, Guangxi Transport Vocational and Technical College, Nanning 530004, China

* Correspondence: qlwei@sdu.edu.cn (Q.W.); chengyu_peng@126.com (C.P.)

Abstract: Lead halide perovskites have been widely used in optoelectronic devices due to their excellent properties; however, the toxicity of lead and the poor stability of these perovskites hinder their further application. Herein, we report a zero-dimensional (0D) lead-free organic manganese (II) bromide hybrid compound of (TBA)₂MnBr₄ (TBA⁺ = tetrabutylammonium cation) single crystals (SCs) with great environmental stability. The (TBA)₂MnBr₄ SCs show a strong green emission peak at 518 nm with a high photoluminescence quantum yield (PLQY) of 84.98% at room temperature, which is attributed to the d-d transition of single Mn²⁺ ions, as also confirmed through density functional calculation. A green light-emitting diode was produced based on (TBA)₂MnBr₄ SCs, which exhibited CIE coordinates (0.17, 0.69) close to those of standard green. A photodetector fabricated by the (TBA)₂MnBr₄ SCs shows an obvious photo response with a rapid millisecond rise/decay response time (at 365 nm). Our findings promote the research of Mn(II)-based organic-inorganic hybrid materials and pave the way by using these materials for future high-performance optoelectronic devices.

Keywords: organic manganese (II) bromide hybrid compound; (TBA)₂MnBr₄; green emission; photodetector; high photoluminescence quantum yield



Citation: Tian, Y.; Wei, Q.; Duan, L.; Peng, C. Lead-Free Organic Manganese (II) Bromide Hybrid with Highly Efficient and Stable Green Emission for UV Photodetection. *Crystals* **2023**, *13*, 1678. <https://doi.org/10.3390/cryst13121678>

Academic Editors: Jérémy Hieulle and Zonghao Liu

Received: 27 November 2023

Revised: 5 December 2023

Accepted: 6 December 2023

Published: 12 December 2023



Copyright: © 2023 by the authors. Licensee MDPI, Basel, Switzerland. This article is an open access article distributed under the terms and conditions of the Creative Commons Attribution (CC BY) license (<https://creativecommons.org/licenses/by/4.0/>).

1. Introduction

As an important semiconductor functional material, lead halide perovskite plays an important role in the light, display, and photodetector fields due to its excellent optoelectronic properties [1–6]. Although lead halide perovskites have achieved a series of remarkable results [7,8], their inherent toxicity and poor stability limit their further applications in optoelectronic devices. Therefore, the key to solving these problems is to explore new non-toxic and stable materials.

Benefiting from structure diversity, low toxicity, and excellent photoluminescence properties, such as tunable luminescence, high photoluminescence quantum yield, and high color purity, Mn(II)-based organic-inorganic hybrid metal halides (OIHMHS) are expected to replace lead halide perovskites and have broad application prospects in the field of optoelectronic devices [9–13]. According to previous studies, the emission of Mn(II)-based OIHMHS originates from the intrinsic d-d transition of Mn²⁺ ions [14–18]. In recent years, many Mn(II)-based OIHMHS have been reported and used to fabricate various optoelectronic devices [19–25]. For example, Chen et al. reported a green light-emitting diode (LED) based on (Ph₄P)₂MnBr₄, with a current efficiency of 32.0 cd A⁻¹, a power efficiency of 26.8 lm W⁻¹, and an external quantum efficiency of 9.6% [20]. Hyunsik et al. also reported a similar green electro-LED based on a 0D [(H₂C=CHCH₂)(C₆H₅)₃P]₂MnBr₄ compound [19], the device performance of which is close to the green device reported by Chen. Except for LED devices, Mn(II)-based compounds are also used in X-ray imaging and scintillators. Ma et al. reported an X-ray scintillator prepared from (C₃₈H₃₄P₂)MnBr₄

powder with a high light yield of about 80,000 photons MeV^{-1} and a low detection limit of 72.8 nGy s^{-1} [25]. Ju et al. reported two kinds of Mn-based compounds with highly efficient luminescence properties; the X-ray scintillators based on these two compounds exhibit high X-ray light yields and low detectable limits, as well as X-ray imaging demonstration with a high resolution [26]. In addition, Mn(II)-based OIHMHS have also been used to fabricate various sensors, such as the fluorescence detection of the pesticide ferbam, acetone vapor, and air humidity [21,23,27]; however, to the best of our knowledge, UV photodetectors fabricated using Mn(II)-based OIHMHS are rarely reported. Therefore, applying Mn(II)-based OIHMHS with excellent optoelectronic properties to UV photodetection is a promising route and beneficial to broaden their applications in the field of optoelectronic devices. This provides a certain reference for the use of non-toxic and stable metal halide materials in the field of photoelectric detection.

In this work, we report a zero-dimensional Mn-based compound, $(\text{TBA})_2\text{MnBr}_4$, which exhibits bright green emission with an emission peak at 518 nm, a full width at half maximum (FWHM) of about 50 nm, and a PLQY as high as 84.98%. The emission mechanism of $(\text{TBA})_2\text{MnBr}_4$ was investigated via steady-state and transient spectroscopy in addition to first-principles calculation, which confirmed that the narrow-band green emission is derived from the d-d transition of the single Mn^{2+} ion. Stability studies show that $(\text{TBA})_2\text{MnBr}_4$ has remarkable stability toward humidity, temperature, and UV light irradiation. In addition, $(\text{TBA})_2\text{MnBr}_4$ powder was coated on a 365 nm UV chip to fabricate the green LED, and the Commission International de l'éclairage (CIE) chromaticity coordinates are (0.17, 0.69), which are close those of standard green. Furthermore, we fabricated a UV photodetector using bulk $(\text{TBA})_2\text{MnBr}_4$ SCs, which exhibited an obvious photo response and a fast response time in the order of milliseconds under excitation at 365 nm. This work promotes the research of Mn(II)-based organic-inorganic hybrid materials and highlights the application potential of these materials in high-performance optoelectronic devices.

2. Results and Discussion

The schematic diagram of the room-temperature liquid-phase diffusion method for growing 0D $(\text{TBA})_2\text{MnBr}_4$ SCs is given in Figure 1a, and a photograph of the various growth stages of $(\text{TBA})_2\text{MnBr}_4$ SCs is shown in Figure S1. Typically, the $\text{C}_{16}\text{H}_{36}\text{NBr}$ and $\text{MnBr}_2 \cdot 4\text{H}_2\text{O}$ were dissolved in a certain amount of ethanol with a molar ratio of 2:1, and a clear pale-yellow precursor solution was obtained via stirring. The toluene was then added to the solution, and the liquid levels of the ethanol precursor liquid and toluene were stratified; however, ethanol gradually diffuses into toluene over time, causing the concentration of the precursor to gradually increase and enter a supersaturated state. As ethanol continues to diffuse into toluene, tiny $(\text{TBA})_2\text{MnBr}_4$ single crystals will precipitate at the junction of the liquid surfaces of ethanol and toluene and gradually grow as ethanol continues to diffuse, finally eventually sinking to the bottom of the glass bottle under the action of gravity. The entire growth cycle is 24 h to 72 h, and the length of the growth time depends on the concentration of the ethanol precursor solution. The greater the concentration of the precursor solution the shorter the growth time, but with correspondingly poorer single-crystal quality. Therefore, the concentration of the ethanol precursor determines the final quality of a single crystal. It is worth noting that we should be careful when adding toluene to the ethanol precursor solution, and to add toluene slowly along the wall of the glass bottle in small amounts and at multiple times; otherwise the toluene and ethanol precursors will mix violently, leading a large number of microcrystals to rapidly precipitate when toluene is added and the force to be too high, finally affecting the growth of single crystals. The optical photograph of $(\text{TBA})_2\text{MnBr}_4$ SCs under daylight and 365 nm UV light in the environmental conditions, as shown in the inset of Figure 1a. The size of the $(\text{TBA})_2\text{MnBr}_4$ SCs obtained through this method is approximately 5 mm. The experimental powder XRD (PXRD) patterns of $(\text{TBA})_2\text{MnBr}_4$ correspond well with the simulation patterns from single-crystal XRD (SCXRD), indicating that the powder sample

is consistent with the SC sample. The $(\text{TBA})_2\text{MnBr}_4$ has a P212121 space group, and the cell parameters are $a = 12.83810 \text{ \AA}$, $b = 12.89970 \text{ \AA}$, $c = 25.08200 \text{ \AA}$, and $\alpha = \beta = \gamma = 90^\circ$. The crystal structure file of $(\text{TBA})_2\text{MnBr}_4$ was obtained from the Cambridge Crystallographic Data Centre (CCDC-1902826). As shown in Figure 1b, the XRD diffraction pattern of the sample obtained through measuring is in good agreement with the simulation results and has no additional diffraction peaks, which proves the successful synthesis of pure $(\text{TBA})_2\text{MnBr}_4$ free of impurities. Each unit cell of $(\text{TBA})_2\text{MnBr}_4$ consists of twenty-one TBA^+ cations and four $[\text{MnBr}_4]^{2-}$ tetrahedra, and all cations are ordered (Figure 1c). As shown in Figure 1d, the distance of the four Mn^{2+} ions in the unit cell varies from 8.951 \AA to 19.928 \AA , which indicates that $(\text{TBA})_2\text{MnBr}_4$ is a typical 0D structure at the molecular level. Moreover, such a large Mn-Mn distance avoids energy transfer interactions between adjacent luminescent centers and ensures that the photogenerated excitons can be effectively bound within the tetrahedral luminescent centers, which is beneficial to the production of efficient luminescence, and the details of this will be provided in the discussion later. A Hitachi SU8020 was used to collect the morphology and elemental distribution of the $(\text{TBA})_2\text{MnBr}_4$ powder samples. The SEM photograph and the elemental mapping images of the powder sample are given in Figure 1e. The size of the powder sample is about 200 \mu m , and the elemental mapping images verified the uniform distribution of Mn and Br. In addition, the atomic ratio of Mn and Br is $8.56:34.89$ ($4.08:1$) when analyzing the proportion of the elements (Figure S2), which is consistent with the theoretical composition of $(\text{TBA})_2\text{MnBr}_4$, indicating the successful synthesis of $(\text{TBA})_2\text{MnBr}_4$.

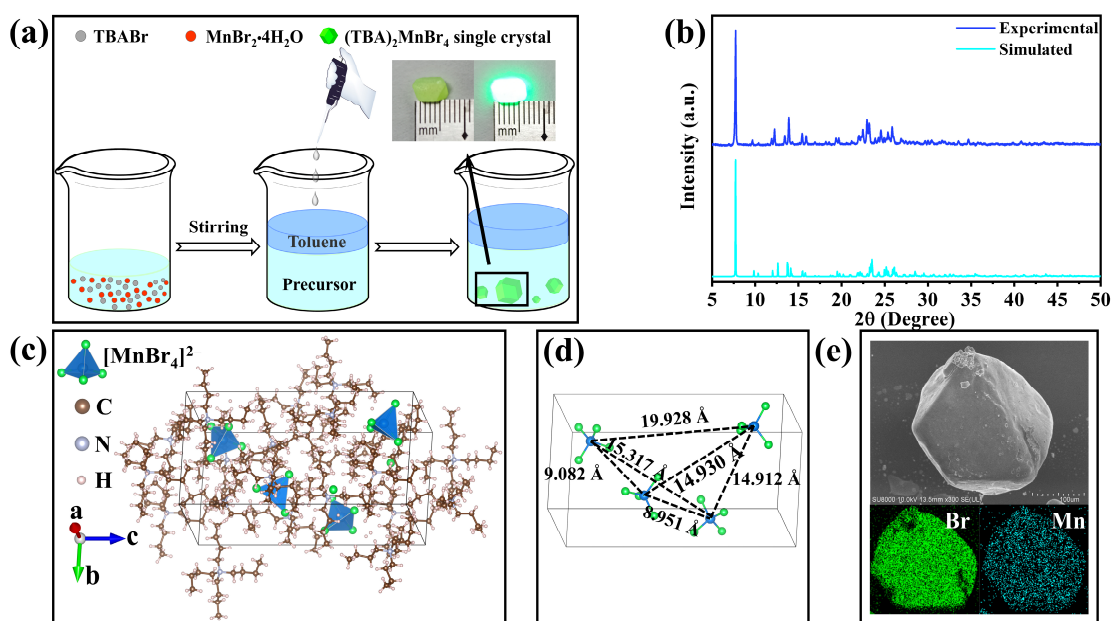


Figure 1. (a) Schematic diagram of the room-temperature liquid-phase diffusion method for growing 0D $(\text{TBA})_2\text{MnBr}_4$ SCs. Insert: The optical photograph of $(\text{TBA})_2\text{MnBr}_4$ SCs under daylight and 365 nm UV light in environmental conditions. (b) PXRD pattern of $(\text{TBA})_2\text{MnBr}_4$ and the corresponding simulated pattern from SCXRD. (c) The crystal structure of $(\text{TBA})_2\text{MnBr}_4$. (d) Diagram of the two adjacent Mn-Mn distances. (e) SEM image of $(\text{TBA})_2\text{MnBr}_4$ micro-crystals and element mapping images of Mn and Br.

In order to deeply understand the inside photophysical properties of $(\text{TBA})_2\text{MnBr}_4$, we carried out steady-state photoluminescence (PL) spectroscopy (Figure 2a) and UV-Vis absorption spectroscopy (Figure S3a) studies on it. Under the 365 nm excitation, the $(\text{TBA})_2\text{MnBr}_4$ shows an emission band centered at 518 nm with an FWHM of 50 nm, which is attributed to the d-d transition (${}^4\text{T}_1(\text{G}) \rightarrow {}^6\text{A}_1(\text{S})$) of single Mn^{2+} ions. Benefitting from the large Mn-Mn distance, the photogenerated excitons are bound within the $[\text{MnBr}_4]^{2-}$

tetrahedra, resulting in a high PLQY (84.98%, Figure S4), which would be discussed in the theoretical calculation. The photoluminescence excitation (PLE) spectra of the emission band centered at 518 nm were also collected, which show seven excitation bands located at ~273 nm, ~288 nm, ~365 nm, ~374 nm, ~433 nm, ~450 nm, and ~468 nm, corresponding to the ${}^6A_1(S) \rightarrow {}^4A_2(F)$, ${}^6A_1(S) \rightarrow {}^4T_1(F)$, ${}^6A_1(S) \rightarrow {}^4E(D)$, ${}^6A_1(S) \rightarrow {}^4T_2(D)$, ${}^6A_1(S) \rightarrow {}^4A_1(G)$, ${}^4E_g(G)$, ${}^6A_1(S) \rightarrow {}^4T_2(G)$, and ${}^6A_1(S) \rightarrow {}^4T_1(G)$ transitions, respectively [16,26,28]. The absorption spectrum of $(TBA)_2MnBr_4$ also shows seven absorption bands (Figure S3a), which are consistent with the PLE spectrum. As shown in Figure S3b, the bandgap value of $(TBA)_2MnBr_4$ is calculated as 2.50 eV according to Tauc's rule: $(\alpha h\nu)^{1/n} = A(h\nu - E_g)$ ($n = 2$ for a direct bandgap and $n = 1/2$ for an indirect bandgap). Figure 2b provides details about the energy absorption and transfer, non-radiative transition, and emission process of a $[MnBr_4]^{2-}$ tetrahedral. Under the excitation of high-energy UV light, the electron absorbs energy and transitions from the ground-state 6A_1 to the high-energy excited state of Mn^{2+} ions and transfers to the 4T_1 energy level through non-radiative transition, finally transitioning back to the ground-state 6A_1 through radiative recombination. Due to the four-coordinate condition, the intensity of the crystal field is weak [29–32]. Therefore, the energy level difference between 4T_1 and the ground-state 6A_1 is large, which ultimately produces a green light emission of 518 nm. Figure 2c presents the PL decay curve of the $(TBA)_2MnBr_4$ under the excitation of 365 nm, monitored at 518 nm at room temperature. The decay curve can be fitted by the following single exponential decay equation [33]:

$$I(t) = I_0 + Ae^{-\frac{t}{\tau}}$$

where $I(t)$ and I_0 are the PL intensity at time t and $t \gg \tau$, A is a constant, and τ is the PL decay time. The PL decay time of $(TBA)_2MnBr_4$ is calculated to be 0.267 ms, which is consistent with that of other reports [19,22,34], further indicating that the green emission of $(TBA)_2MnBr_4$ originates from the d-d transition (${}^4T_1(G) \rightarrow {}^6A_1(S)$) of a single $[MnBr_4]^{2-}$ tetrahedron. Figure 2d shows the Raman spectra of $(TBA)_2MnBr_4$ excited by a 633 nm laser at room temperature. The Raman modes at a low wavenumber ($<400 \text{ cm}^{-1}$) come from the vibrations of a $[MnBr_4]^{2-}$ tetrahedron [16,30,35], and the vibrations of tetrabutylammonium cations are located at high wavenumbers [36]; the detailed Raman peak positions and corresponding Raman mode assignments are listed in Table S1. The strongest Raman mode is located at 80.43 cm^{-1} . This is usually associated with acoustics with polaron properties [37]. Furthermore, it is worth noting that the Raman mode at 152.89 cm^{-1} can be viewed as the overtone of the 80.43 cm^{-1} , and the Raman mode at 253.59 cm^{-1} can be approximately regarded as the triple frequency of the 80.43 cm^{-1} mode, which indicates the presence of multi-phonon modes in $(TBA)_2MnBr_4$, indicating strong electron–phonon coupling [37].

Key information such as crystal field strength, electron–phonon interactions, etc., can be obtained through temperature-dependent PL spectroscopy [38,39]. Herein, we used 365 nm ultraviolet light as the excitation source and collected the PL spectrum of $(TBA)_2MnBr_4$ single crystals in the temperature range of 80 K–360 K. As shown in Figure 3a, all of the PL peaks shift towards a lower energy direction with increasing temperature (from 509 nm to 529 nm), and are accompanied by spectral broadening. This phenomenon is contrary to the blue shift of the PL peaks with an increase in the temperature of Mn-based organic–inorganic hybrid metal halides reported in other works in the literature [17,40,41]. Since the ${}^4T_1(G) \rightarrow {}^6A_1(S)$ transition energy is inversely proportional to the crystal field strength [42], the crystal field strength of $(TBA)_2MnBr_4$ at room temperature is higher than 80 K. At 360 K, the PL intensity of $(TBA)_2MnBr_4$ is about 60% of the PL intensity at 80 K (Figure 3b), indicating that $(TBA)_2MnBr_4$ has high thermal stability and good thermal quenching resistance, which makes it expected to be applied in the field of solid-state lighting. To further determine the thermal stability of $(TBA)_2MnBr_4$, we fit the binding energy (E_b) using the Arrhenius formula [43]:

$$I(t) = I_0 / Ae^{-E_b/k_B T}$$

where I_0 is the PL intensity at 0 K, $I(t)$ is the PL intensity at temperature T , A is a constant, E_b is the binding energy, and k_b is the Boltzmann constant. The binding energy obtained as a function of PL intensity and temperature is 39.43 meV (Figure 3c), which is larger than the room temperature thermal energy (about 26 meV). The high activation energy (E_b) of $(\text{TBA})_2\text{MnBr}_4$ makes it difficult for the excited electrons to overcome the nonradiative transition energy barrier, thus ensuring the excellent thermal stability of $(\text{TBA})_2\text{MnBr}_4$. To study the interaction between electrons and lattice vibrations in $(\text{TBA})_2\text{MnBr}_4$, we calculated the Huang–Rhys factor, S , of $(\text{TBA})_2\text{MnBr}_4$. The Huang–Rhys factor, S , can be solved by using the following formula [44]:

$$\text{FWHM}(T) = 2.36\hbar\omega \sqrt{S \coth\left(\frac{\hbar\omega}{2k_B T}\right)} \quad (1)$$

where $\hbar\omega$ is the phonon energy and k_b is the Boltzmann constant. The hyperbolic function, $\coth(x)$, can be expressed as follows:

$$\coth(x) = \frac{e^x + e^{-x}}{e^x - e^{-x}} = 1 + \frac{1}{e^{2x} - 1} \quad (2)$$

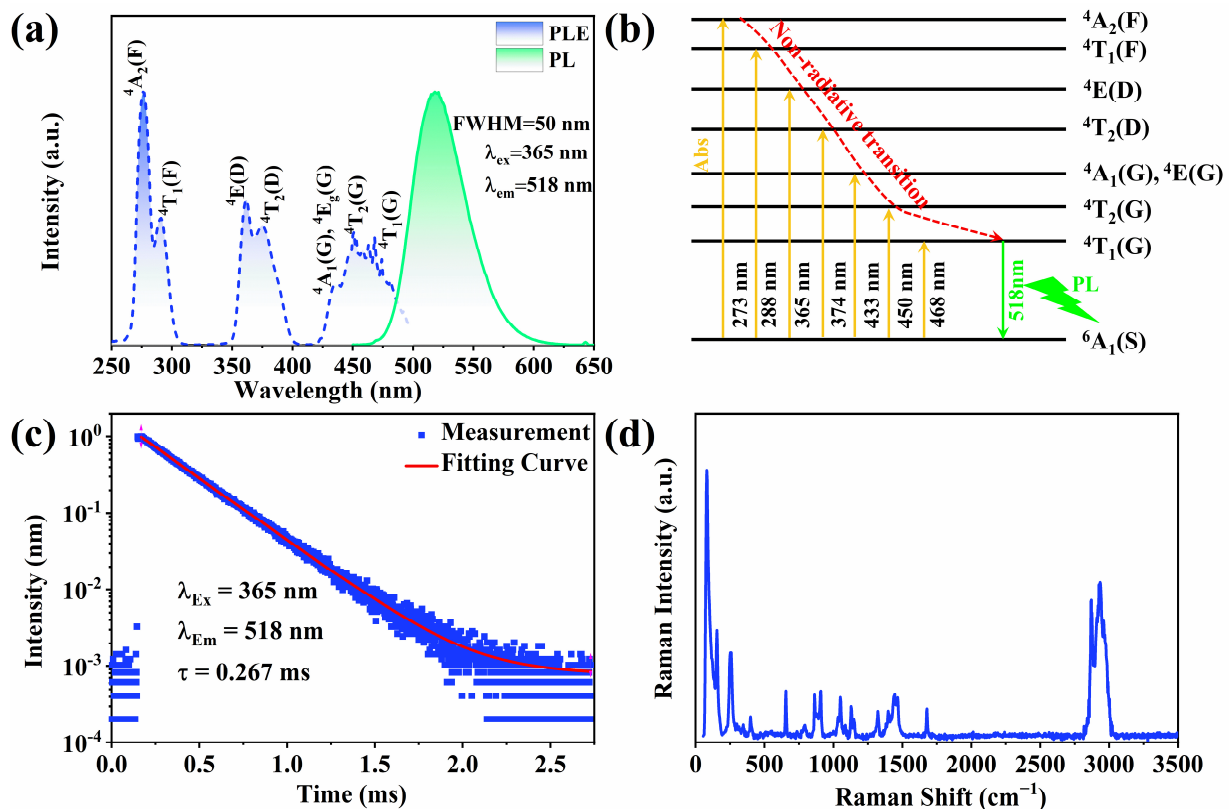


Figure 2. (a) The PLE and PL spectra of $(\text{TBA})_2\text{MnBr}_4$. (b) The schematic diagram about energy absorption and transfer, non-radiative transition, and emission process of $(\text{TBA})_2\text{MnBr}_4$. (c) The PL decay curve of $(\text{TBA})_2\text{MnBr}_4$ under excitation at 365 nm and monitored at 518 nm. (d) The Raman spectra of $(\text{TBA})_2\text{MnBr}_4$ excitation via a 633 nm laser at room temperature.

Therefore, Equation (1) can be written as follows:

$$\text{FWHM}(T) = 2.36\hbar\omega \sqrt{S \left(1 + \frac{1}{e^{\frac{\hbar\omega}{k_b T}} - 1}\right)} \quad (3)$$

$$\text{FWHM}^2(T) = 5.57 \times S \times (\hbar\omega)^2 \left(1 + \frac{1}{e^{\frac{\hbar\omega}{k_b T}} - 1} \right) \quad (4)$$

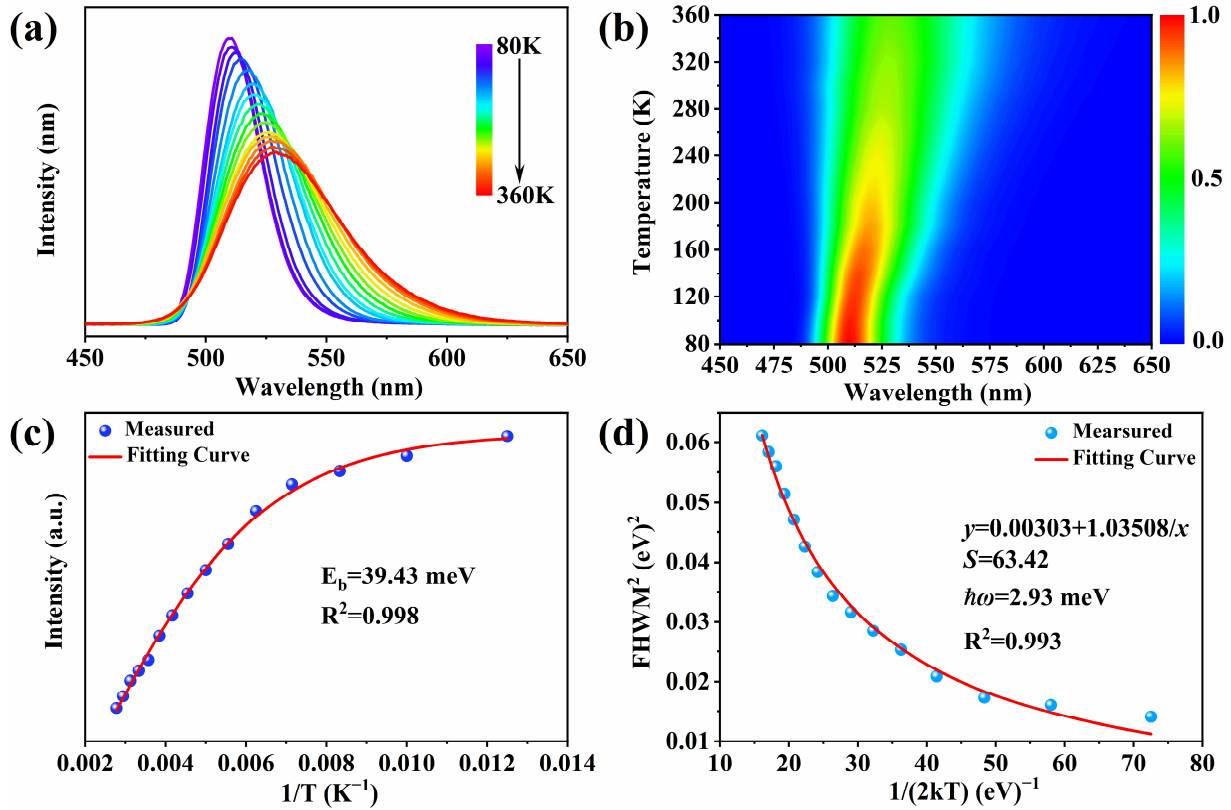


Figure 3. (a) Temperature-dependent PL spectra of $(\text{TBA})_2\text{MnBr}_4$ under the excitation wavelength of 365 nm. (b) Pseudo-color maps of temperature-dependent PL spectra. (c) PL intensity vs. $1/T$ and the fitting result. (d) FWHM^2 vs. $1/(2kT)$ and the fitting result.

When $\frac{\hbar\omega}{k_b T}$ is small enough, $e^{\frac{\hbar\omega}{k_b T}} - 1$ can be approximately expressed as $\frac{\hbar\omega}{2k_b T}$; therefore, Equation (4) can be written as follows:

$$\text{FWHM}^2(T) = 5.57 \times S \times (\hbar\omega)^2 \left(1 + \frac{1}{\frac{\hbar\omega}{2k_b T}} \right) \quad (5)$$

This can be further expressed as follows:

$$\text{FWHM}^2(T) = a + \frac{b}{\frac{1}{2k_b T}} \quad (6)$$

where $a = 5.57 \times S \times (\hbar\omega)^2$ and $b = 5.57 \times S \times (\hbar\omega)$. The Huang–Rhys factor, S , defines the degree of electron–phonon coupling [16,17]. The value of $\frac{1}{2k_b T}$ and FWHM^2 can be obtained according to the PL spectrum from 80 K to 360 K. As shown in Figure 3d, taking $\frac{1}{2k_b T}$ as the horizontal axis and FWHM^2 as the vertical axis, the Huang–Rhys factor, S , and phonon energy, $\hbar\omega$, are obtained by fitting, corresponding to $S = 63.42$ and $\hbar\omega = 2.93$ meV. Such a large S may be related to the organic cations in $(\text{TBA})_2\text{MnBr}_4$. According to the research of Sargent et al., electron–phonon interaction is related to the stiffness of organic cations; greater stiffness of the organic cations leads to stronger lattice vibration, and the corresponding electron–phonon interaction will be stronger [44]. Due to the tetrabutylammonium

cation having four C-C-C-C chains, belonging to soft organic cations with rigidity, which can generate strong lattice vibration, the result is a large S . The large Huang–Rhys factor, S , indicates that $(\text{TBA})_2\text{MnBr}_4$ has strong electron–phonon coupling, which is consistent with the results obtained through Raman spectroscopy.

Density functional theory (DFT) calculations were used to deeply understand the PL mechanism and electronic structure of $(\text{TBA})_2\text{MnBr}_4$. The energy band structure of $(\text{TBA})_2\text{MnBr}_4$ is shown in Figure 4a; $(\text{TBA})_2\text{MnBr}_4$ exhibits flat band edges, indicating that $(\text{TBA})_2\text{MnBr}_4$ has highly localized electronic states, consistent with the electronic structure of 0D organic–inorganic hybrid metal halides [40,45]. Furthermore, the flat bands of both the valence band maximum (VBM) and the conduction band minimum (CBM) indicate that no obvious intermolecular coupling within a $[\text{MnBr}_4]^{2-}$ tetrahedron can be found, which proves that each $[\text{MnBr}_4]^{2-}$ tetrahedron can be regarded as an independent emission center [21], which is the key to producing highly efficient luminescence [46]. At the same time, the large Mn^{2+} ions' distance ensures that there is no obvious energy transfer between adjacent $[\text{MnBr}_4]^{2-}$ tetrahedral luminescent centers, ultimately producing efficient green light emission. The calculated bandgap of $(\text{TBA})_2\text{MnBr}_4$ at the Γ point in the Brillouin zone is about 2.52 eV, which is consistent with the experimental bandgap value (2.50 eV). Figure 4b shows the calculated total of each element's orbital-resolved partial densities of states (DOSs); the valence band maximum (VBM) is composed of Mn-3d and Br-4p orbitals and the conduction band minimum (CBM) is composed of Mn-3d orbitals, while the organic molecules do not contribute to the frontier orbitals, which indicates that the bandgap of $(\text{TBA})_2\text{MnBr}_4$ is determined by the inorganic $[\text{MnBr}_4]^{2-}$ tetrahedron. The large-sized tetrabutylammonium bromide organic molecules play a role in supporting the skeleton and effectively isolating the $[\text{MnBr}_4]^{2-}$ tetrahedral luminescent center in the structure. In addition, the sharp peaks near the VBM and CBM indicate that the valence and conduction bands of $(\text{TBA})_2\text{MnBr}_4$ are almost dispersion-free, indicating negligible electronic coupling within $[\text{MnBr}_4]^{2-}$ [47].

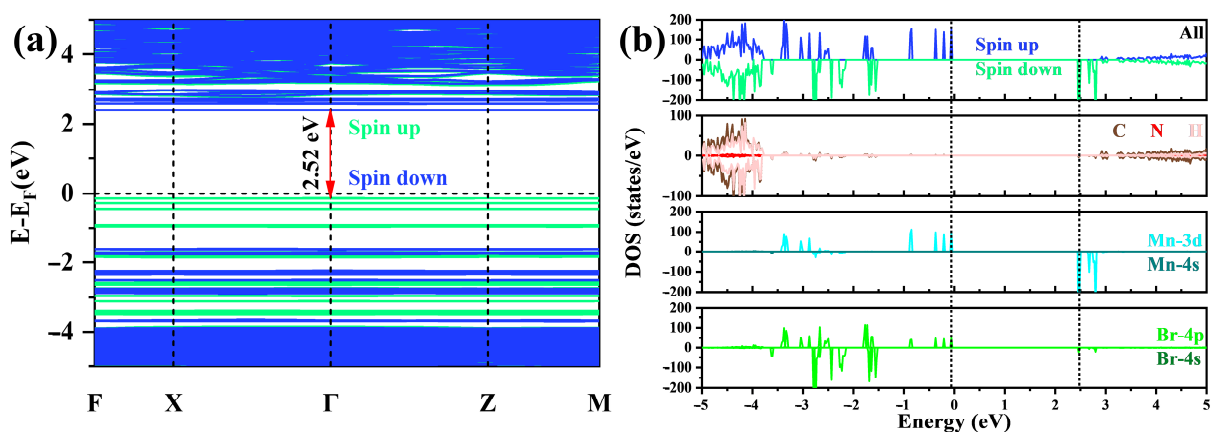


Figure 4. The energy band structure (a) and density of state (b) of $(\text{TBA})_2\text{MnBr}_4$.

The stability of materials is crucial for the fabrication of high-performance optoelectronic devices. Before fabricating optoelectronic devices using $(\text{TBA})_2\text{MnBr}_4$ SCs, we first evaluated the stability of $(\text{TBA})_2\text{MnBr}_4$ SCs. As shown in Figure S5a, the PXRD pattern of $(\text{TBA})_2\text{MnBr}_4$ showed that no additional diffraction peaks were generated and that there was no shift in diffraction peaks compared with as-synthesized samples after they are stored for 60 days in ambient conditions ($T \approx 30^\circ\text{C}$ and $\text{RH} \approx 70\%$). The TGA measurement found that the initial decomposition temperature of $(\text{TBA})_2\text{MnBr}_4$ is about 220°C , indicating that $(\text{TBA})_2\text{MnBr}_4$ has a high thermal stability (Figure S5b). The $(\text{TBA})_2\text{MnBr}_4$ can still maintain a high PLQY after being stored for 60 days in ambient conditions, about 90% of that of the as-synthesized samples (Figure S5c). In addition, the PL intensity of the sample attenuated by about 5% after 4 h of UV irradiation, indicating that $(\text{TBA})_2\text{MnBr}_4$ has high UV stability

(Figure S5d). The above results show that $(\text{TBA})_2\text{MnBr}_4$ has excellent stability and is very suitable for the preparation of high-performance optoelectronic devices.

The efficient luminescence properties and excellent stability of $(\text{TBA})_2\text{MnBr}_4$ make it a promising green phosphor for solid-state lighting applications [48]. Therefore, $(\text{TBA})_2\text{MnBr}_4$ powder was coated on the 365 nm GaN UV chip, and a bright green light was obtained after switching on the power, as shown in the insert of Figure S6a. To compare the green emission of the $(\text{TBA})_2\text{MnBr}_4$ with standard green light, their CIE coordinates, through the use of a CIE chromaticity diagram based on the PL spectrum, were collected. The coordinates of the green emission of $(\text{TBA})_2\text{MnBr}_4$ are (0.17, 0.69), which are close to those of standard green (Figure S6a). Meanwhile, with an increase in voltage or current the spectral shape remains almost unchanged (Figure S6b,c), indicating that $(\text{TBA})_2\text{MnBr}_4$ has excellent stability and great application potential as a green phosphor.

Bulk single crystals with a narrow bandgap, high carrier mobility, and steady-state photocurrent are excellent candidates for the fabrication of high-performance photosensitive devices [49–52]. According to our literature survey on the optoelectronic applications of manganese-based metal halides in recent years, Mn(II)-based metal halides are currently mainly used in the fields of X-ray scintillators, LEDs, and sensors, while reports in the field of photodetectors are still rare. Table S2 summarizes the main application directions of typical Mn(II)-based metal halides in recent years. Based on this, we used the as-grown large-sized $(\text{TBA})_2\text{MnBr}_4$ single crystals to prepare ultraviolet photodetectors to explore the application potential of this type of material in the field of photodetectors. A UV photodetector with a planar metal–crystal–metal structure of $\text{Ag}/(\text{TBA})_2\text{MnBr}_4/\text{Ag}$ is shown in the inset of Figure 5b. The quality of $(\text{TBA})_2\text{MnBr}_4$ SCs was first evaluated before characterizing the performance of the device. The density of trap states (n_{trap}) is an important indicator for evaluating the quality of a single crystal [53]. The silver paste was brushed on both sides of the $(\text{TBA})_2\text{MnBr}_4$ SCs with a thickness of 3.5 mm as electrodes (inset of Figure 5a), and the I–V curve was tested under dark conditions. As shown in Figure 5a, the dark I–V curve can be divided into three parts on the log–log scale: (1) the Ohmic region ($I \propto V^{n=1}$, $V < 56.72$ V)—in this region the current increases linearly with voltage; (2) the Child’s region ($I \propto V^{n=2}$, $V > 66.83$ V)—in this region the current exhibits quadratic voltage; and (3) the trap fill limited (TFL) region ($I \propto V^{n=1}$, 56.72 V $< V < 66.83$ V). The voltage value at the inflection points between the Ohmic region and the TFL region is called the trap fill limited voltage (V_{TFL}), and the n_{trap} can be defined by the following formula [47]:

$$V_{\text{TFL}} = \frac{ed^2n_{\text{trap}}}{2\epsilon\epsilon_0}$$

where e is the elemental charge, $d = 3.5$ mm is the thickness of $(\text{TBA})_2\text{MnBr}_4$ SCs, ϵ is the relative dielectric constant of $(\text{TBA})_2\text{MnBr}_4$ SCs, and ϵ_0 is the vacuum permittivity. A Tonghui TH2828 precision LCR meter was used to measure the capacitance of the $\text{Ag}/(\text{TBA})_2\text{MnBr}_4/\text{Ag}$ device, and the $\epsilon = 28.5$ is calculated by the formula $\epsilon = \frac{Ct}{\epsilon_0 A}$, where $A = 1.44 \times 10^{-6}$ m² is the area of the Ag electrodes. Therefore, the trap density, n_{trap} , is estimated to be about 1.46×10^{10} cm⁻². The lower trap density indicates that $(\text{TBA})_2\text{MnBr}_4$ SCs have the quality of high crystallinity, making them an ideal material for fabricating photodetectors. Unfortunately, due to the weak excitation intensity of the xenon lamp, we could not observe the obvious optoelectronic signal of the device with excitation by the xenon lamp. Therefore, a fixed-wavelength laser ($\lambda = 365$ nm) was utilized as an excitation source with which to study the optoelectronic properties of the $(\text{TBA})_2\text{MnBr}_4$ device. The I–V curves of the device under dark and light conditions are shown in Figure 5b, and the device exhibits a distinct photo response after being excited by UV light compared to dark conditions. The I–V curve of the device shows relatively symmetrical characteristics. Here, we defined the rectification ratio as the ratio between the forward bias current and reverse bias current [54]. Therefore, the rectification ratio of the device is approximately equal to 1 here. The time-dependent photocurrent response of the $(\text{TBA})_2\text{MnBr}_4$ device is shown in Figure 5c. After multiple on–off cycles, the device can still work stably, with

high reproducibility. Benefiting from the high crystalline quality, the grain boundary recombination of carriers is reduced [55], and the on–off ratio of the device is 8.73 under an electrode distance of about 5 mm. Therefore, the on–off ratio can be further improved if the distance between electrodes is further narrowed or a more suitable electrode material is selected [40,56]. The rise time (t_{rise}) and decay time (t_{fall}) were calculated to be 103.91 ms and 98.02 ms, respectively, close to the values of previously reported Mn-based metal halide photodetectors [56]. The fast photo response of the device was attributed to the high quality of the $(\text{TBA})_2\text{MnBr}_4$ SCs. Our results promote the research of Mn(II)-based organic–inorganic hybrid materials and highlight the application potential of these materials in high-performance optoelectronic devices.

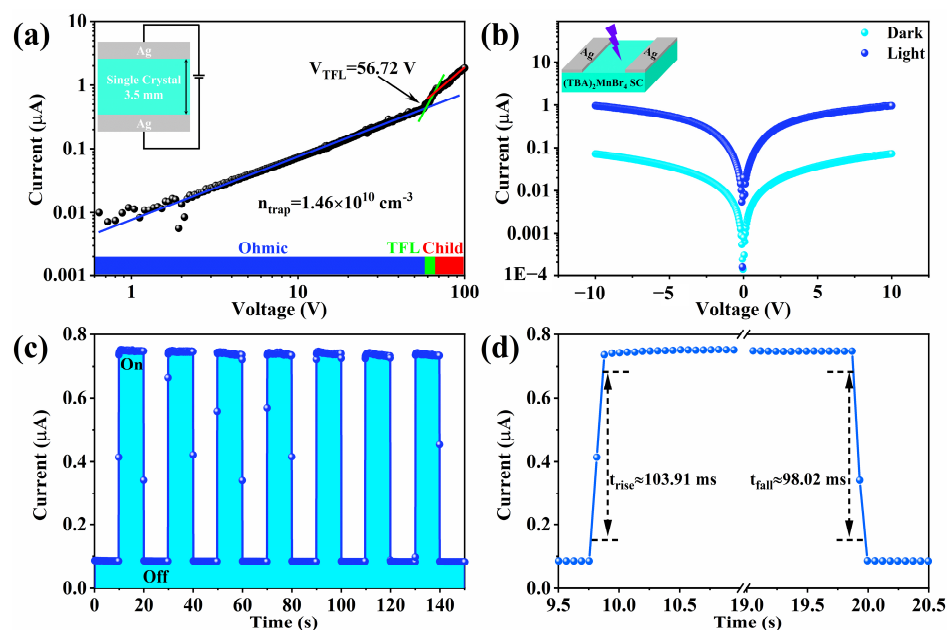


Figure 5. (a) I–V curve to calculate the trap density of $(\text{TBA})_2\text{MnBr}_4$ SCs. (b) I–V curve collected in the dark and with a 365 nm laser. (c) The on–off curve of the $(\text{TBA})_2\text{MnBr}_4$ device under the 365 nm laser with bias voltage of 10 V. (d) Rising and decay edges of the $(\text{TBA})_2\text{MnBr}_4$ device.

3. Conclusions

In conclusion, we synthesized a new lead-free 0D Mn(II)-based organic–inorganic hybrid metal bromide $(\text{TBA})_2\text{MnBr}_4$. This compound exhibits strong green emission with peaking at 518 nm, which is attributed to the d-d transition of the single Mn^{2+} ion. In addition, the as-synthesized $(\text{TBA})_2\text{MnBr}_4$ shows a high PLQY of 84.98% and remarkable stability toward humidity, temperature, and UV irradiation. Meanwhile, a green LED was fabricated via coated $(\text{TBA})_2\text{MnBr}_4$ on the 365 nm UV chip, and the coordinates of the green emission of $(\text{TBA})_2\text{MnBr}_4$ are (0.17, 0.69), which are close those of standard green. Finally, a UV photodetector based on bulk $(\text{TBA})_2\text{MnBr}_4$ SCs was fabricated, which exhibits a distinct positive photo response and a fast response time in the order of milliseconds. Our results promote the research of Mn(II)-based organic–inorganic hybrid materials and pave the way by using these materials for future high-performance optoelectronic devices.

Supplementary Materials: The following supporting information can be downloaded at: <https://www.mdpi.com/article/10.3390/cryst13121678/s1>, Figure S1: The photograph of the growth process of $(\text{TBA})_2\text{MnBr}_4$ SCs. Figure S2: The Energy disperse spectrum of $(\text{TBA})_2\text{MnBr}_4$. Figure S3: The UV-Vis absorption spectrum (a) of $(\text{TBA})_2\text{MnBr}_4$ and corresponding Tauc plot (b). Figure S4: The PLQY measurement view of $(\text{TBA})_2\text{MnBr}_4$ shows that the PLQY is as high as 84.98%. The excitation wavelength was 365 nm. Figure S5: (a) The XRD patterns of $(\text{TBA})_2\text{MnBr}_4$ before and after stored in ambient condition for 60 days. (b) TGA curve of $(\text{TBA})_2\text{MnBr}_4$. (c) The PLQY value variation of $(\text{TBA})_2\text{MnBr}_4$. (d) Long-term PL stability of $(\text{TBA})_2\text{MnBr}_4$ under a 365 nm UV lamp within 4 h.

Figure S6: (a) The CIE coordinates of the fabricated LED. Emission spectra of the fabricated LED at different driving voltage (b) and currents (c). Table S1: Assignments of the observed Raman spectra of $(\text{TBA})_2\text{MnBr}_4$ SCs. Table S2: The main optoelectronic application directions of typical Mn(II)-based metal halides. References [19,21,28,40,57–63] are cited in the Supplementary Materials.

Author Contributions: Software, Q.W.; investigation, L.D.; writing—original draft preparation, Y.T.; writing—review and editing, C.P. All authors have read and agreed to the published version of the manuscript.

Funding: National Natural Science Foundation of China (grant no. 62175219) and the open research fund of the State Key Laboratory of Dynamic Testing Technology (grant no. 2022-SYSJJ-01).

Data Availability Statement: The data presented in this study are available in the Supplementary Materials.

Acknowledgments: This work was financially supported by the National Natural Science Foundation of China (grant no. 62175219) and the open research fund of the State Key Laboratory of Dynamic Testing Technology (grant no. 2022-SYSJJ-01).

Conflicts of Interest: The authors declare no conflict of interest.

References

1. Cortecchia, D.; Yin, J.; Petrozza, A.; Soci, C. White Light Emission in Low-Dimensional Perovskites. *J. Mater. Chem. C* **2019**, *7*, 4956–4969. [[CrossRef](#)]
2. Chen, Z.; Zhao, J.; Zeng, R.; Liu, X.; Zou, B.; Xiang, W. High Efficiency Fluorescent Perovskite Quantum Dots Encapsulated in Superhydrophobic Silica Aerogel for Wide Color Gamut Backlight Displays. *Chem. Eng. J.* **2022**, *433*, 133195. [[CrossRef](#)]
3. Chen, Q.; Wu, J.; Ou, X.; Huang, B.; Almutlaq, J.; Zhumekenov, A.A.; Guan, X.; Han, S.; Liang, L.; Yi, Z.; et al. All-Inorganic Perovskite Nanocrystal Scintillators. *Nature* **2018**, *561*, 88–93. [[CrossRef](#)]
4. Xuan, T.; Xie, R.-J. Recent Processes on Light-Emitting Lead-Free Metal Halide Perovskites. *Chem. Eng. J.* **2020**, *393*, 124757. [[CrossRef](#)]
5. Bao, C.; Yang, J.; Bai, S.; Xu, W.; Yan, Z.; Xu, Q.; Liu, J.; Zhang, W.; Gao, F. High Performance and Stable All-Inorganic Metal Halide Perovskite-Based Photodetectors for Optical Communication Applications. *Adv. Mater.* **2018**, *30*, 1803422. [[CrossRef](#)]
6. Miao, J.; Zhang, F. Recent Progress on Highly Sensitive Perovskite Photodetectors. *J. Mater. Chem. C* **2019**, *7*, 1741–1791. [[CrossRef](#)]
7. Afroz, M.A.; Singh, A.; Gupta, R.K.; Garai, R.; Tailor, N.K.; Choudhary, S.; Sharma, B.; Mahajan, P.; Padha, B.; Verma, S. Design Potential and Future Prospects of Lead-free Halide Perovskites in Photovoltaic Devices. *J. Mater. Chem. A* **2023**, *11*, 13133–13173. [[CrossRef](#)]
8. Parikh, N.; Akin, S.; Kalam, A.; Prochowicz, D.; Yadav, P. Probing the Low-Frequency Response of Impedance Spectroscopy of Halide Perovskite Single Crystals Using Machine Learning. *ACS Appl. Mater. Interfaces* **2023**, *15*, 27801–27808. [[CrossRef](#)]
9. Wang, B.; Wang, C.; Chu, Y.; Zhang, H.; Sun, M.; Wang, H.; Wang, S.; Zhao, G. Environmental-Friendly Lead-Free Chiral Mn-Based Metal Halides with Efficient Circularly Polarized Photoluminescence at Room Temperature. *J. Alloys Compd.* **2022**, *910*, 164892. [[CrossRef](#)]
10. He, Z.-L.; Wei, J.-H.; Luo, J.-B.; Zhang, Z.-Z.; Kuang, D.-B. Reversible Human-Temperature-Responsive Luminescence Switching in A Mn(II)-Based Metal Halide. *J. Mater. Chem. C* **2023**, *11*, 1251–1257. [[CrossRef](#)]
11. Liang, D.; Xiao, H.; Cai, W.; Lu, S.; Zhao, S.; Zang, Z.; Xie, L. Mn^{2+} -Based Luminescent Metal Halides: Syntheses, Properties, and Applications. *Adv. Opt. Mater.* **2023**, *11*, 2202997. [[CrossRef](#)]
12. Dai, G.; Ma, Z.; Qiu, Y.; Li, Z.; Fu, X.; Jiang, H.; Ma, Z. A Red-Emitting Hybrid Manganese Halide Perovskite $\text{C}_5\text{H}_5\text{NOMnCl}_2 \cdot \text{H}_2\text{O}$ Featuring One-Dimensional Octahedron Chains. *Inorg. Chem.* **2022**, *61*, 12635–12642. [[CrossRef](#)]
13. Shimono, S.; Sekine, M.; Niwa, Y.; Sagayama, H.; Araki, K.; Hata, Y.; Kishimura, H. Solid-Liquid Transitions in Mn-Based Ionic Liquids $[\text{MeIM}]_2[\text{MnBr}_4]$ and $[\text{EtIM}]_2[\text{MnBr}_4]$ Producing Emission Spectra with Narrow Green Bands. *Mater. Res. Bull.* **2023**, *159*, 112103. [[CrossRef](#)]
14. Kou, T.; Wei, Q.; Jia, W.; Chang, T.; Peng, C.; Liang, Y.; Zou, B. Light Emission Enhancement of $(\text{C}_3\text{H}_{10}\text{N})_4\text{Pb}_{1-x}\text{Mn}_x\text{Br}_6$ Metal-Halide Powders by the Dielectric Confinement Effect of a Nanosized Water Layer. *ACS Appl. Mater. Interfaces* **2022**, *14*, 6167–6179. [[CrossRef](#)]
15. Yu, Z.; Peng, H.; Wei, Q.; Huang, T.; Yao, S.; Tian, Y.; Peng, C.; Zou, B. The Magnetic Molaron Modulated Luminescence Manders of Organic-Inorganic Hybrid Ferroelectric Anti-Perovskite $(\text{C}_3\text{H}_9\text{N})_3\text{Cd}_2\text{Cl}_7$ Doped with Mn^{2+} . *Mater. Today Chem.* **2022**, *24*, 100781. [[CrossRef](#)]
16. Zhang, S.; Zhao, Y.; Zhou, J.; Ming, H.; Wang, C.-H.; Jing, X.; Ye, S.; Zhang, Q. Structural Design Enables Highly-Efficient Green Emission with Preferable Blue Light Excitation from Zero-Dimensional Manganese (II) Hybrids. *Chem. Eng. J.* **2021**, *421*, 129886. [[CrossRef](#)]

17. Zhou, G.; Ding, J.; Jiang, X.; Zhang, J.; Molokeev, M.S.; Ren, Q.; Zhou, J.; Li, S.; Zhang, X.-M. Coordination Units of Mn²⁺ Modulation Toward Tunable Emission in Zero-Dimensional Bromides for White Light-Emitting Diodes. *J. Mater. Chem. C* **2022**, *10*, 2095–2102. [[CrossRef](#)]
18. Liu, H.L.; Ru, H.Y.; Sun, M.E.; Wang, Z.Y.; Zang, S.Q. Organic–Inorganic Manganese Bromide Hybrids with Water-Triggered Luminescence for Rewritable Paper. *Adv. Opt. Mater.* **2021**, *10*, 2101700. [[CrossRef](#)]
19. Jana, A.; Sree, V.G.; Ba, Q.; Cho, S.C.; Lee, S.U.; Cho, S.; Jo, Y.; Meena, A.; Kim, H.; Im, H. Efficient Organic Manganese(II) Bromide Green-Light-Emitting Diodes Enabled by Manipulating the Hole and Electron Transport Layer. *J. Mater. Chem. C* **2021**, *9*, 11314–11323. [[CrossRef](#)]
20. Xu, L.J.; Sun, C.Z.; Xiao, H.; Wu, Y.; Chen, Z.N. Green-Light-Emitting Diodes based on Tetrabromide Manganese(II) Complex through Solution Process. *Adv. Mater.* **2017**, *29*, 1605739. [[CrossRef](#)] [[PubMed](#)]
21. Li, M.; Zhou, J.; Molokeev, M.S.; Jiang, X.; Lin, Z.; Zhao, J.; Xia, Z. Lead-Free Hybrid Metal Halides with a Green-Emissive [MnBr₄] Unit as a Selective Turn-On Fluorescent Sensor for Acetone. *Inorg. Chem.* **2019**, *58*, 13464–13470. [[CrossRef](#)]
22. Su, B.; Molokeev, M.S.; Xia, Z. Mn²⁺-Based Narrow-Band Green-Emitting Cs₃MnBr₅ Phosphor and The Performance Optimization by Zn²⁺ Alloying. *J. Mater. Chem. C* **2019**, *7*, 11220–11226. [[CrossRef](#)]
23. Chen, S.; Gao, J.; Chang, J.; Zhang, Y.; Feng, L. Organic-Inorganic Manganese (II) Halide Hybrids Based Paper Sensor for The Fluorometric Determination of Pesticide Ferbam. *Sens. Actuators B-Chem.* **2019**, *297*, 126701. [[CrossRef](#)]
24. Wang, S.; Han, X.; Kou, T.; Zhou, Y.; Liang, Y.; Wu, Z.; Huang, J.; Chang, T.; Peng, C.; Wei, Q.; et al. Lead-Free Mn^{II}-Based Red-Emitting Hybrid Halide (CH₆N₃)₂MnCl₄ Toward High Performance Warm WLEDs. *J. Mater. Chem. C* **2021**, *9*, 4895–4902. [[CrossRef](#)]
25. Xu, L.J.; Lin, X.; He, Q.; Worku, M.; Ma, B. Highly Efficient Eco-Friendly X-Ray Scintillators Based on An Organic Manganese Halide. *Nat. Commun.* **2020**, *11*, 4329. [[CrossRef](#)]
26. Jiang, T.; Ma, W.; Zhang, H.; Tian, Y.; Lin, G.; Xiao, W.; Yu, X.; Qiu, J.; Xu, X.; Yang, Y.; et al. Highly Efficient and Tunable Emission of Lead-Free Manganese Halides toward White Light-Emitting Diode and X-Ray Scintillation Applications. *Adv. Funct. Mater.* **2021**, *31*, 2009973. [[CrossRef](#)]
27. Gao, W.; Leng, M.; Hu, Z.; Li, J.; Li, D.; Liu, H.; Gao, L.; Niu, G.; Tang, J. Reversible Luminescent Humidity Chromism of Organic-Inorganic Hybrid PEA₂MnBr₄ Single Crystals. *Dalton Trans.* **2020**, *49*, 5662–5668. [[CrossRef](#)]
28. Hu, G.; Xu, B.; Wang, A.; Guo, Y.; Wu, J.; Muhammad, F.; Meng, W.; Wang, C.; Sui, S.; Liu, Y.; et al. Stable and Bright Pyridine Manganese Halides for Efficient White Light-Emitting Diodes. *Adv. Funct. Mater.* **2021**, *31*, 2011191. [[CrossRef](#)]
29. Li, C.; Luo, Z.; Liu, Y.; Wei, Y.; He, X.; Chen, Z.; Zhang, L.; Chen, Y.; Wang, W.; Liu, Y. Self-Trapped Exciton Emission with High Thermal Stability in Antimony-Doped Hybrid Manganese Chloride. *Adv. Opt. Mater.* **2022**, *10*, 2102746. [[CrossRef](#)]
30. Zhao, X.; Wu, M.; Liu, H.; Wang, Y.; Wang, K.; Yang, X.; Zou, B. Pressure-Treated Engineering to Harvest Enhanced Green Emission in Mn-Based Organic–Inorganic Metal Halides at Ambient Conditions. *Adv. Funct. Mater.* **2022**, *32*, 2109277. [[CrossRef](#)]
31. Zhang, R.; Xie, H.; Liu, W.; Zhan, K.; Liu, H.; Tang, Z.; Yang, C. High-Efficiency Narrow-Band Green-Emitting Manganese (II) Halide for Multifunctional Applications. *ACS Appl. Mater. Interfaces* **2023**, *15*, 47238–47249. [[CrossRef](#)] [[PubMed](#)]
32. Wang, N.; Xiong, Y.; Liu, K.; He, S.; Cao, J.; Zhang, X.; Zhao, J.; Liu, Q. Efficient Narrow-Band Green Light-Emitting Hybrid Halides for Wide Color Gmut Display. *ACS Appl. Electron. Mater.* **2022**, *4*, 4068–4076. [[CrossRef](#)]
33. Zhou, G.; Liu, Z.; Huang, J.; Molokeev, M.S.; Xiao, Z.; Ma, C.; Xia, Z. Unraveling the Near-Unity Narrow-Band Green Emission in Zero-Dimensional Mn²⁺-Based Metal Halides: A Case Study of (C₁₀H₁₆N)₂Zn_{1-x}Mn_xBr₄ Solid Solutions. *J. Phys. Chem. Lett.* **2020**, *11*, 5956–5962. [[CrossRef](#)] [[PubMed](#)]
34. Fu, P.; Sun, Y.; Xia, Z.; Xiao, Z. Photoluminescence Behavior of Zero-Dimensional Manganese Halide Tetrahedra Embedded in Conjugated Organic Matrices. *J. Phys. Chem. Lett.* **2021**, *12*, 7394–7399. [[CrossRef](#)] [[PubMed](#)]
35. Barreda-Argueso, J.A.; Nataf, L.; Rodriguez-Lazcano, Y.; Aguado, F.; Gonzalez, J.; Valiente, R.; Rodriguez, F.; Wilhelm, H.; Jephcoat, A.P. Bulk and Molecular Compressibilities of Organic-Inorganic Hybrids [(CH₃)₄N]₂MnX₄ (X = Cl, Br); Role of Intermolecular Interactions. *Inorg. Chem.* **2014**, *53*, 10708–10715. [[CrossRef](#)] [[PubMed](#)]
36. Mao, W.; Wang, J.; Hu, X.; Zhou, B.; Zheng, G.; Mo, S.; Li, S.; Long, F.; Zou, Z. Synthesis, Crystal Structure, Photoluminescence Properties of Organic-Inorganic Hybrid Materials Based on Ethylenediamine Bromide. *J. Saudi Chem. Soc.* **2020**, *24*, 52–60. [[CrossRef](#)]
37. Peng, C.; Wei, Q.; Yao, S.; Meng, X.; Yu, Z.; Peng, H.; Zhong, X.; Zou, B. H₂O–NH₄⁺-Induced Emission Modulation in Sb³⁺-Doped (NH₄)₂InCl₅·H₂O. *Inorg. Chem.* **2022**, *61*, 12406–12414. [[CrossRef](#)]
38. Jin, P.; Fu, Y.; Niu, R.; Zhang, Q.; Zhang, M.; Li, Z.; Zhang, X. Non-Destructive Detection of the Freshness of Air-Modified Mutton Based on Near-Infrared Spectroscopy. *Foods* **2023**, *12*, 2756. [[CrossRef](#)]
39. Qiu, Y.; Shi, M.; Guo, X.; Li, J.; Wu, J.; Zhou, Y.; Sun, H.; Hang, Y.; Li, X.; Li, Y. Sensitivity Improvement in the Measurement of Minor Components by Spatial Confinement in Fiber-Optic Laser-Induced Breakdown Spectroscopy. *Spectrochim. Acta Part B* **2023**, *209*, 106800. [[CrossRef](#)]
40. Wu, Y.; Fan, W.; Gao, Z.; Tang, Z.; Lei, L.; Sun, X.; Li, Y.; Cai, H.-L.; Wu, X. New Photoluminescence Hybrid Perovskites with Ultrahigh Photoluminescence Quantum Yield and Ultrahigh Thermostability Temperature up to 600 K. *Nano Energy* **2020**, *77*, 105170. [[CrossRef](#)]
41. Artem'ev, A.V.; Davydova, M.P.; Berezin, A.S.; Sukhikh, T.S.; Samsonenko, D.G. Photo- and Triboluminescent Robust 1D Polymers Made of Mn(II) Halides and Meta-Carborane Based Bis(Phosphine Oxide). *Inorg. Chem. Front.* **2021**, *8*, 2261–2270. [[CrossRef](#)]

42. Sugano, S. *Multiplets of Transition-Metal Ions in Crystals*; Elsevier: Amsterdam, The Netherlands, 2012.
43. Jing, Y.; Liu, Y.; Jiang, X.; Molokeev, M.S.; Lin, Z.; Xia, Z. Sb³⁺ Dopant and Halogen Substitution Triggered Highly Efficient and Tunable Emission in Lead-Free Metal Halide Single Crystals. *Chem. Mater.* **2020**, *32*, 5327–5334. [[CrossRef](#)]
44. Gong, X.; Voznyy, O.; Jain, A.; Liu, W.; Sabatini, R.; Piontkowski, Z.; Walters, G.; Bappi, G.; Nokhrin, S.; Bushuyev, O.; et al. Electron-Phonon Interaction in Efficient Perovskite Blue Emitters. *Nat. Mater.* **2018**, *17*, 550–556. [[CrossRef](#)] [[PubMed](#)]
45. Li, Z.; Zhang, C.; Li, B.; Lin, C.; Li, Y.; Wang, L.; Xie, R.-J. Large-Scale Room-Temperature Synthesis of High-Efficiency Lead-Free Perovskite Derivative (NH₄)₂SnCl₆:Te Phosphor for Warm wLEDs. *Chem. Eng. J.* **2021**, *420*, 129740. [[CrossRef](#)]
46. Kong, L.; Liu, Y.; Dong, L.; Zhang, L.; Qiao, L.; Wang, W.; You, H. Enhanced Red Luminescence in CaAl₁₂O₁₉:Mn⁴⁺ via Doping Ga³⁺ for Plant Growth Lighting. *Dalton Trans.* **2020**, *49*, 1947–1954. [[CrossRef](#)] [[PubMed](#)]
47. Mo, X.; Li, T.; Huang, F.; Li, Z.; Zhou, Y.; Lin, T.; Ouyang, Y.; Tao, X.; Pan, C. Highly-Efficient All-Inorganic Lead-Free 1D CsCu₂I₃ Single Crystal for White-Light Emitting Diodes and UV Photodetection. *Nano Energy* **2021**, *81*, 105570. [[CrossRef](#)]
48. Zhong, J.; Han, M.; Li, C.; Li, R.; He, H. Facile and Scalable Fabrication Process of Electroluminescent Filament with High Luminescent Efficiency. *Mater. Lett.* **2023**, *350*, 134868. [[CrossRef](#)]
49. Zhou, G.; Liu, Z.; Molokeev, M.S.; Xiao, Z.; Xia, Z.; Zhang, X.-M. Manipulation of Cl/Br Transmutation in Zero-Dimensional Mn²⁺-Based Metal Halides Toward Tunable Photoluminescence and Thermal Quenching Behaviors. *J. Mater. Chem. C* **2021**, *9*, 2047–2053. [[CrossRef](#)]
50. Pasupuleti, K.S.; Reddeppa, M.; Park, B.-G.; Oh, J.-E.; Kim, S.-G.; Kim, M.-D. Efficient Charge Separation in Polypyrrole/GaN-Nanorod-Based Hybrid Heterojunctions for High-Performance Self-Powered UV Photodetection. *Phys. Status Solidi RRL* **2021**, *15*, 2000518. [[CrossRef](#)]
51. Vuong, V.-H.; Pammi, S.; Ippili, S.; Jella, V.; Thi, T.N.; Pasupuleti, K.S.; Kim, M.-D.; Jeong, M.J.; Jeong, J.-R.; Chang, H.S. Flexible, Stable, and Self-Powered Photodetectors Embedded with Chemical Vapor Deposited Lead-Free Bismuth Mixed Halide Perovskite Films. *Chem. Eng. J.* **2023**, *458*, 141473. [[CrossRef](#)]
52. Wang, H.; Li, Z.; Li, D.; Chen, P.; Pi, L.; Zhou, X.; Zhai, T. Van der Waals Integration Based on Two-Dimensional Materials for High-Performance Infrared Photodetectors. *Adv. Funct. Mater.* **2021**, *31*, 2103106. [[CrossRef](#)]
53. Balderas-Aguilar, J.U.; Falcony, C.; Garduño-Wilchis, I.A.; Aguilar-Frutis, M.; Hernandez-Como, N.; Martínez-Merlín, I.E.; García-Hipólito, M.; Alonso-Huitrón, J.C. All-Green Cs₄CuSb₂Cl₁₂ Perovskite Films Deposited in Situ by AACVD and Their Doping with F-Ions for Photodetectors and Memdiodes. *J. Mater. Chem. C* **2023**, *11*, 16214–16224. [[CrossRef](#)]
54. Afzal, A.M.; Javed, Y.; Akhtar Shad, N.; Iqbal, M.Z.; Dastgeer, G.; Munir Sajid, M.; Mumtaz, S. Tunneling-Based Rectification and Photoresponsivity in Black Phosphorus/Hexagonal Boron Nitride/Rhenium Diselenide Van der Waals Heterojunction Diode. *Nanoscale* **2020**, *12*, 3455–3468. [[CrossRef](#)] [[PubMed](#)]
55. Liu, Y.; Zhang, Y.; Zhao, K.; Yang, Z.; Feng, J.; Zhang, X.; Wang, K.; Meng, L.; Ye, H.; Liu, M.; et al. A 1300 mm² Ultrahigh-Performance Digital Imaging Assembly using High-Quality Perovskite Single Crystals. *Adv. Mater.* **2018**, *30*, 1707314. [[CrossRef](#)] [[PubMed](#)]
56. Shao, L.; Zhou, D.; Ding, N.; Sun, R.; Xu, W.; Wang, N.; Xu, S.; Liu, D.; Song, H. Broadband Ultraviolet Photodetectors Based on Cerium Doped Lead-Free Cs₃MnBr₅ Metal Halide Nanocrystals. *ACS Sustain. Chem. Eng.* **2021**, *9*, 4980–4987. [[CrossRef](#)]
57. Luo, J.B.; Wei, J.H.; Zhang, Z.Z.; He, Z.L.; Kuang, D.B. A Melt-Quenched Luminescent Glass of an Organic–Inorganic Manganese Halide as a Large-Area Scintillator for Radiation Detection. *Angew. Chem. Int. Ed.* **2023**, *135*, e202216504. [[CrossRef](#)]
58. Zhang, W.; Sui, P.; Zheng, W.; Li, L.; Wang, S.; Huang, P.; Zhang, W.; Zhang, Q.; Yu, Y.; Chen, X. Pseudo-2D Layered Organic-Inorganic Manganese Bromide with a Near-Unity Photoluminescence Quantum Yield for White Light-Emitting Diode and X-Ray Scintillator. *Angew. Chem. Int. Ed.* **2023**, *135*, e202309230. [[CrossRef](#)]
59. Shao, W.; Zhu, G.; Wang, X.; Zhang, Z.; Lv, H.; Deng, W.; Zhang, X.; Liang, H. Highly Efficient, Flexible, and Eco-Friendly Manganese (II) Halide Nanocrystal Membrane with Low Light Scattering for High-Resolution X-ray Imaging. *ACS Appl. Mater. Interfaces* **2023**, *15*, 932–941. [[CrossRef](#)]
60. Li, B.; Xu, Y.; Zhang, X.; Han, K.; Jin, J.; Xia, Z. Zero-Dimensional Luminescent Metal Halide Hybrids Enabling Bulk Transparent Medium as Large-Area X-Ray Scintillators. *Adv. Opt. Mater.* **2022**, *10*, 2102793. [[CrossRef](#)]
61. Li, C.; Wu, D.; Wang, Q.; Bai, Y.; He, P.; An, K.; Tang, X. Lead-Free Scintillators Based on Pyridine Manganese Halide for X-ray Imaging. *J. Lumin.* **2022**, *250*, 119130. [[CrossRef](#)]
62. Kong, Q.; Meng, X.; Ji, S.; Wang, Q.; Yang, B.; Bai, T.; Wang, X.; Wang, Z.; Zhang, R.; Zheng, D. Highly Reversible Cesium Manganese Iodine for Sensitive Water Detection and X-ray Imaging. *ACS Mater. Lett.* **2022**, *4*, 1734–1741. [[CrossRef](#)]
63. Sree, V.G.; Jana, A.; Cho, S.C.; Lee, S.U.; Cho, S.; Sohn, J.I.; Im, H. Green and Warm-White Light-Emitting Diodes Enabled by Zero-Dimensional Green-Emitting Mn(II) Bromide Complex with Record High Efficiency. *Chem. Eng. J.* **2023**, *474*, 145936. [[CrossRef](#)]

Disclaimer/Publisher's Note: The statements, opinions and data contained in all publications are solely those of the individual author(s) and contributor(s) and not of MDPI and/or the editor(s). MDPI and/or the editor(s) disclaim responsibility for any injury to people or property resulting from any ideas, methods, instructions or products referred to in the content.